M.R. Drinkwater
Jet Propulsion Laboratory, California Institute of Technology, Pasadena, California, USA

D.G. Long & D.S. Early
Electrical and Computer Engineering Department, Brigham Young University, Provo, Utah, USA

Enhanced-Resolution ERS-1 Scatterometer Imaging of Southern-Ocean Sea Ice

Abstract A new method of image reconstruction is described which allows enhanced-resolution images to be produced from gridded C-band scatterometer data from the Active Microwave Instrument (AMI) carried by ESA's ERS-1 satellite. Resulting images are weekly averages which improve the nominal resolution of 50 km to an enhanced resolution of approximately 14 km. Time-integrated images are maps of the mean radar-backscatter coefficient normalised to 40° incidence. Such medium-scale images are derived for application to mapping the dynamics of the Southern-Ocean sea-ice cover. These all-weather day and night images may be derived in regions of the globe from AMI scatterometer-mode data where higher resolution (25 m) AMI SAR image data are unavailable due to the lack of a local SAR receiving station, or during periods when the receiving station is closed.

Results demonstrate that this enhanced-resolution imaging technique applied to the scatterometer mode of the AMI complements and considerably enhances the lower frequency temporal and spatial coverage of high-resolution SAR images in the Antarctic.

1. Introduction

To date, the principal focus for measurements in the scatterometer mode of the ESA ERS-1 satellite's Active Microwave Instrument (AMI) has been the estimation of ocean surface wind vectors. Although such low-bit-rate data are acquired continuously when the Synthetic-Aperture Radar (SAR) imaging mode is not being used, this information has barely been exploited outside the traditional scope of wind speed and direction measurement. Further applications are limited largely because of the preference for the higher resolution that the AMI SAR mode and other sources of data offer.

The extensive coverage of the ERS-1 scatterometer is particularly valuable due to the lack of data reception in the AMI SAR mode when no receiving station is available. This is especially true in the Arctic and Antarctic, where portions of the northern- and southern-hemisphere sea-ice covers are currently not imaged by SAR. In the case of the Antarctic, it is presently impossible to obtain microwave image information on the extent and characteristics of the Southern-Ocean sea ice at times when the O'Higgins and Syowa SAR receiving stations are not operating. Similarly, a large portion of the Southern-Ocean sea-ice cover is not imaged in the Pacific sector, owing to the lack of a SAR receiving station in this locality.

Operationally, it is not possible to obtain sufficient SAR images in a short enough time span to be able to effectively map sea-ice conditions. In this paper we propose a method using data acquired using the alternative scatterometer mode of the AMI instrument onboard ERS-1 for mapping sea-ice characteristics over the whole Southern Ocean's sea-ice cover. This method allows the construction of relatively higher resolution scatterometer images from the backscatter data and, by virtue of the wider swath and larger coverage of the scatterometer-mode data, allows mapping of the entire sea-ice cover in the space of one week. The result is a weekly average sea-ice picture, for comparison with the SSM/I passive microwave sea-ice products, which can be used to track regional-scale spatial and temporal changes in the sea-ice cover around the entire Antarctic coast. Since the spatial resolution is a factor of 2 or more higher than with passive microwave data, this approach also allows features and mean large-scale sea-ice dynamics to be more effectively tracked. Multiple azimuth- and incidence-angle scatterometer measurements aid in simple ice-boundary identification[1] and also ice-properties discrimination[2].

2. Filling the gaps

One of the priorities for scientific studies of polar ice and snow is high spatial and temporal coverage. The exploitation of SAR data, particularly in studies related to the mapping and monitoring of the sea-ice cover, has been one of the main driving forces behind inclusion of that instrument onboard ERS-1[3]. A large number of sea-ice studies are currently being performed using the SAR data received at a number of northern-hemisphere ground stations (such as Fairbanks in Alaska and Kiruna in Sweden). These SAR receiving stations enable the majority of the northern-hemisphere sea-ice cover to be mapped using the SAR. However, significant volumes of data are required to map the complete Arctic on a weekly basis, and such a monitoring goal is currently beyond the resources of on/off time allocated to this high-power, high-bit-rate instrument. Correspondingly less coverage is possible for the more extensive sea-ice cover around Antarctica. The extent of the two receiving masks of the currently operable German and Japanese Antarctic receiving stations, and the operating times during which these stations can receive data, are presently limited. The result is a high-resolution SAR image database which is at best discontinuous in space and time.

A key advantage of the ERS-1 scatterometer mode (EScat) from the AMI instrument is that it operates whenever the AMI SAR is switched off and it retrieves information from the Antarctic sea-ice cover without needing a direct downlink receiving station. The wider EScat swath also provides more frequent, multiple-incidence-angle coverage in a given location. This Low Bit Rate (LBR) data source is essential for filling in the gaps in both space and time for the Antarctic ice cover. Until now, the intrinsic low resolution of the EScat data is the main reason why they have not been used in such applications. Nevertheless, the approach described below

introduces a technique that can produce weekly maps of the entire Southern-Ocean sea-ice cover at a resolution higher than present alternatives such as the SSM/I passive microwave radiometers. Resulting backscatter images are based on multiple azimuth- and incidence-angle observations, which are also helpful in ice-characteristic discrimination and the separation of ice from ocean.

3. High-resolution scatterometer imaging

Traditionally, spaceborne scatterometers have been low-resolution radars designed to measure winds over the ocean. This trend began with the successful but short-lived Seasat-A satellite scatterometer (SASS). Improved resolution would enhance the utility of the scatterometer data for ice and land studies. Here we introduce a method for obtaining enhanced-resolution images of normalised radar backscatter in the ERS-1 scatterometer (EScat) mode of the AMI. While this technique has been developed using Seasat scatterometer (SASS) data[4], it is also applicable to the ERS-1 instrument data. The approach is based upon the spatial overlap achieved by the instrument over a period of time (multiple orbits), generating higher resolution images than the original resolution of 50 km.

3.1. ERS-1 AMI scatterometer data

The EScat makes 5.3 GHz (C-band) measurements of linear vertically (VV) co-polarised backscatter (σ°) on ascending and descending orbits at various azimuth (from mid, fore and aft beams) and incidence angles. The location of instantaneous measurement cells is determined in the across-track direction by gating the received echo, and in the along-track direction by timing of transmit pulses. Cross-track resolution is obtained by a combination of the narrow-beam pattern, the antenna illumination pattern azimuth-angle geometry, and the range-gating. Along-track resolution is determined by the combination of a narrow antenna pattern, the accuracy of transmit pulse timing and the integration and averaging of successive along-track echoes. The resulting resolution is nominally 50 km.

A series of pulses are integrated and spatially filtered to yield the 50 km resolution σ° measurements on a 25 km grid. As each beam successively sweeps over a given grid cell node location, the overlapping integration measurement-cell measurements from each of the three antennas are recorded for that grid location. Using this measurement and gridding approach, the location accuracy (along- and across-track) of each cell measurement is around ± 25 km. However, the number and relative positions of the pulses integrated into the σ° measurement is variable. Every few orbits, the spacecraft will pass over this region again on either an ascending or descending ground track. This results in crossing measurement swaths with multiple overlapping measurements. During the 35-day repeat (Phase-C) orbit cycle, the orbit precession shifts the pattern of measurements meridionally, effectively providing coverage of the entire Earth's surface. In general, a given area at high latitudes is observed several times each day with varying azimuth and incidence angles.

Sea-ice backscatter is a function of the measurement incidence angle, θ, and geophysical properties of the ice[2]. The dependence of σ° on θ can be expressed as

$$\sigma^\circ(\theta) = \alpha_0^A \{\beta_0(\theta)\}^B \tag{1}$$

with

$$\alpha_0 = 10^{1/10} \tag{2}$$

$$\beta_0(\theta) = 10^{(40-\theta)/10} \tag{3}$$

In the incidence angle range $18^\circ \leq \theta \leq 59^\circ$ corresponding to EScat measurements, σ° (in dB) is approximately a linear function of θ (Ref. 5)

$$\sigma^\circ(\theta) = A + B(\theta - 40^\circ) \tag{4}$$

where the coefficients A and B depend on surface characteristics and azimuth angle (ϕ). A is the 40° incidence-angle-normalised σ°, while B describes the dependence of σ° on θ. Due to the wide range in θ, we will use A and B in the following discussion rather than σ°. In Equation (1), 40° represents the mean θ of the observations and is thus a convenient angle for making comparative data analyses.

Over sea ice, σ° is not significantly affected by the azimuth angle ϕ of the observations. Livingstone & Drinkwater[5] observe typically less than 1.0 dB azimuthal modulation (about the mean) when examining C-band sea-ice σ° over a 360° range in ϕ. For a given sea-ice area, SASS measurements also show negligible azimuthal modulation in σ°. Lecomte et al.[1] utilise this finding in their derivation of a measure of the azimuthal isotropy of the backscatter from fore and aft beam measurements. Practical use of such a measure has shown some value in the recognition and discrimination of the sea-ice margin from the open ocean. Typically, the open ocean illustrates the condition of azimuthal anisotropy, owing to the fact that wind-generated ripples are aligned with the direction of the wind. In subsequent processing, σ° was therefore assumed to have no azimuth-angle modulation. Ignoring such modulation is recognised as a limitation or drawback in this current work, as open-water or low-ice-concentration areas may be present within the pack, where wind-generated capillary waves then result in widely varying σ° between each of the three beams. With respect to the polarisation of the data used in this study, the EScat retrieved σ° data at fixed (linear) vertical transmit and receive polarisation (VV-pol). This is in contrast to the SASS instrument, which was capable of measurements at two like polarisations (VV- and HH-pol). Because of this diffeence, for the purpose of SASS and EScat data comparisons we limit graphical presentation of results to VV polarisation only.

3.2. The resolution-enhancement and image-reconstruction technique

A recently developed technique for enhancing the resolution of scatterometer data can be used to create images of A at finer resolutions than the intrinsic 50 km resolution of scatterometer data. The complete scatterometer image reconstruction algorithm with filtering (SIRF) is described in greater detail by Long et al.[4]. This technique utilises multiple, overlapping measurements of σ° and post-processing to improve the resolution. SIRF provides images of A and B with a resolution of up to 4−5 km from originally 50 km-resolution SASS data[4,6]. The resolution enhancement for EScat is somewhat less than for SASS data (see comments on the restrictions and trade-offs in resolution below).

The SIRF approach is based upon first an enhanced-resolution model for creating images of A and B, and second a reconstructive technique optimised for noisy scatterometer measurements. Both components take advantage of spatial overlap in the measurements made at different times with different beams. Broadly, the enhanced-resolution σ° model utilises a small-scale rectilinear grid of resolution elements on the Earth's surface of size $S_c \times S_a$ in the cross-track (c) and along-track (a) directions. As the fore, mid and aft beams successively sweep over the grid, the overlapping integration-measurement-cell measurements of each of the three antennas are superimposed upon the grid elements[4]. The estimated value of backscatter $\hat{\sigma}_n^\circ$ for the n^{th} measurement is then a weighted average of the σ° values of the individual resolution elements covered by the integration measurement cell:

$$\hat{\sigma}_n^\circ = \sum_{c=L_n}^{R_n} \sum_{a=B_n}^{T_n} h(c,a;n)\ \alpha_0^{A(c,a)}\ [\beta_0(\theta_n)]^{B(c,a)} \tag{5}$$

Summation limits are defined by a rectangle bounding the n^{th} σ° measurement cell which has top and bottom limits T_n and B_n, and left and right limits L_n and R_n. In the first term of Equation (5), the weighting function $h(c,a;n)$ is the effective instrument measurement response (where $0 \le h \le 1$), while in the second term the incidence-angle dependence of $\hat{\sigma}_n^\circ$ is expressed in terms of β_0, from Equation (3).

Since actual scatterometer measurements are noisy, the technique is extended to include its effect. A modified, multivariate multiplicative algebraic reconstruction

technique (MART) is applied in the determination of the high-resolution estimates of $A(c,a)$ and $B(c,a)$. The result is enhanced-resolution images of A and B, where each grid resolution element becomes a pixel in the reconstructed image.

3.3. Imaging trade-offs

In this study, the resulting image pixel resolution is chosen to be $0.33° \times 0.125°$ (i.e. 3 pixels per degree of longitude by 8 pixels per degree of latitude) or approximately 12.5×13.9 km at a latitude of 70°S. This resolution enhancement from 50 km to ~14 km is not without cost since, for instance, variance in the A or B images increases as resolution is increased. A trade-off is made between the resolution and the noise level with multiple passes over the target being required to obtain sufficient measurement overlap for the reconstruction algorithm to yield an improvement in resolution. The absolute resolution improvement depends on the total number of measurements, with greater numbers contributing to a reduced estimate of noise and/or improved resolution. However, during the 'imaging time interval', the radar and surface characteristics must remain constant between passes. Some trade-off must therefore be made between imaging time interval and resolution, due to temporal change. Additional requirements are imposed and additional assumptions made regarding the $\sigma°$ measurements:

(i) Instrument calibration must remain stable over the data-acquisition interval.
(ii) $\sigma°$ is assumed independent of the azimuth angle of the measurement.
(iii) Surface topographic effects on the image-reconstruction process are assumed negligible for sea ice. Thus, surface slope modification of the local incidence angle and modelling of its influence upon estimation of A and B is ignored.
(iv) A and B are assumed to remain constant over the imaging time interval. For a sufficiently short interval, this assumption is justified. However, the interval must be several days to a week in order to obtain the measurement overlap required for the highest possible resolution with full coverage of Antarctica.

Large long-term seasonal changes are observed in A and B in sea-ice regions over a full ice growth year in the Southern Ocean. In contrast, however, the large-scale relative change in $\sigma°$ over 1 to 2 weeks is relatively small, and so we restrict the imaging interval to 1 week. A 7-day imaging time interval provides the best trade-off between coverage and resolution. Resulting images reflect the average or 'filtered' sea-ice backscatter response during this imaging time period. Variations in $\sigma°$ during each 1-week interval are treated as noise by the image-reconstruction algorithm. Short-term variability observed on time scales of 1−5 days caused by ice motion, melting and refreezing, or precipitation events, is averaged out. Thus the effects of high-frequency changes in the backscatter, consistent with passing storms and moving low-pressure systems, are not evident in the images displayed here. These effects are effectively removed in the high-resolution data, with the result that only the longer time-scale changes due to the large-scale sea-ice dynamics remain in the weekly image variations.

A major drawback of this approach is the assumption that sea-ice motion and decorrelation of gridded backscatter (due to motion effects) is not an important effect in terms of image reconstruction. While this assumption is recognised to be a limitation of results presented in this study, these effects are currently under further investigation. Measurements of sea-ice floe drift rates in the western Weddell Sea by Argos buoys and a drifting ice station (Fig. 9), however, indicate typical mean drift speeds of around 10 ± 7 km/day, or the equivalent of 70 ± 49 km/week. Such motion is the equivalent of an $\sim 5 \pm 3$ pixel gridding error in the reconstructed weekly images and this effect smoothes any remaining high-frequency pixel variability in the final images.

Unfortunately, EScat provides limited time-of-day diversity, with measurements restricted to two local imaging times which vary with location. Seasat SASS studies of $\sigma°$ as a function of time-of-day in several regions over the Greenland ice sheet[7] indicated no significant diurnal effects on the reconstructed images. This is probably due to insufficient time-of-day diversity in the data, and so diurnal variations are not considered here.

Detailed studies using synthetic images[4] and SASS data from the tropical rain forests[6] show that the resulting errors in estimating A are generally less than 1 dB. To reduce errors as far as possible, measurements with excessive noise (i.e. those with normalised standard deviations greater than 15%) are not used in the imaging process. Data from orbits with large spacecraft attitude errors are also rejected. Long et al.[4] give a further discussion of data anomalies and error filtering used in the SIRF algorithm.

Thus, for EScat the effective resolution enhancement is dependent on the spatial overlap of the measurements from different passes, the response of the spatial filter applied to the original pulse measurements, and the spatial accuracy of the gridded scatterometer data. Note that the actual amount of data and the data overlap are dependent on the switching on and off of the AMI modes. Using SASS data, a resolution enhancement of 8−10 times (6 km) was achieved. In contrast, a reduced resolution enhancement of 3−4 times (14 km) is achieved with the EScat due to the poorer spatial accuracy of these measurements and the uncertain individual pulse locations. It is apparent in subsequent image examples that there are periods and geographic locations where insufficient EScat data are collected for A values to be generated: these appear as black pixels in the images. The resulting medium-scale images nonetheless have significant application to sea-ice geophysical studies, and examples are illustrated in the following sections.

4. Southern-Ocean sea-ice mapping

The ability of the SIRF algorithm to produce images of the sea-ice characteristics around the whole Antarctic Continent is demonstrated in Figures 1 and 2. Figure 1 is an image of the sea-ice at nearly the minimum ice extent, during the first week of February 1992 (Julian Days 32−39). Figure 2 shows the contrasting situation near maximum ice extent at the end of September (Julian Days 272−278). Each sea-ice map is illustrated as the normalised incidence-angle value A of radar backscatter at 40°. Both figures indicate the smoothly varying isotropic returns from the sea ice relative to the highly variable and anisotropic returns of the ocean beyond the sea-ice margin around Antarctica (due to backscattering from wind-generated waves). The residual Antarctic sea-ice cover in the Amundsen, Bellingshausen and Weddell Seas is clearly visible in Figure 1 as bright patches extending northwards from the Antarctic coast. Figure 2 clearly shows the regions of greatest ice extent during winter, with the lower mean A values of winter sea-ice evident. Note the contrastingly greater structure observed within this extensive sea-ice cover, with particularly strong swirls and bands observed in the backscatter values of the Weddell Sea.

The C-band backscatter at this incidence angle largely reflects the salinity and roughness of the sea ice[2,8]. Both of these sea-ice geophysical properties are related to the age of the sea ice and its history of deformation throughout a single ice season. Another factor may be snow depth, which is also related to the age of the ice since formation. Summer A values in Figure 1 reach −10 dB, owing to predominantly rough-surface scattering from ice floes during wet surface conditions. In contrast, the mean winter A values in Figure 2 decrease, as a higher salinity first-year ice cover grows rapidly to latitudes north of 60°S near the Greenwich meridian. Samples of the Weddell Sea A values from the winter ice cover indicate a typical variation in C-band backscatter between −5 and −30 dB. This range in values reflects the structure and variability in the sea-ice cover of this region[8]. One further feature of Figure 2 is the bright fringe clearly observed in the Pacific sector around the marginal sea-ice zone. Similar high-backscatter values were measured in the Weddell Sea in June with a scatterometer during the Winter Weddell Gyre Study, and it is suggested that these returns correspond with pancake ice formation during high wave activity at the edge of the pack-ice.

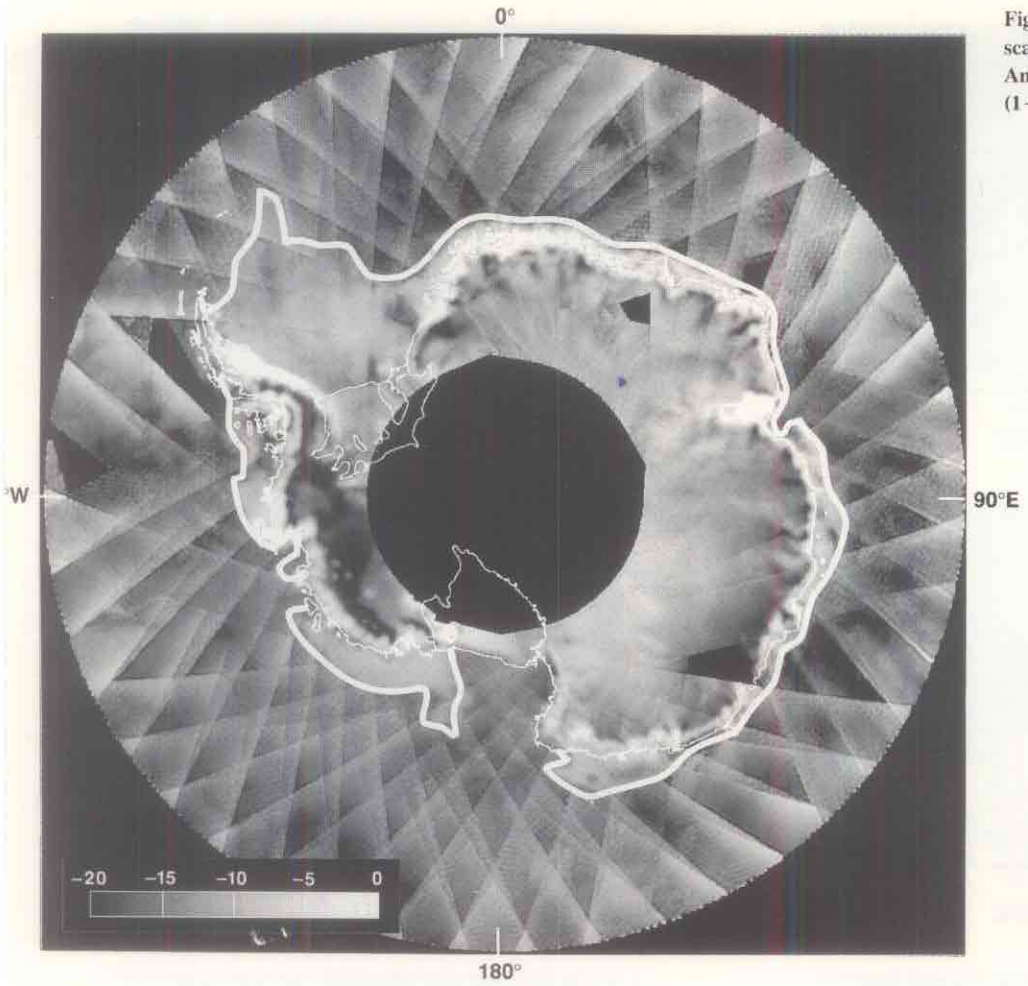

Figure 1. Reconstructed ERS-1 AMI scatterometer 14 km resolution *A* image of the Antarctic sea-ice extent in austral summer (1−7 Feb. 1992)

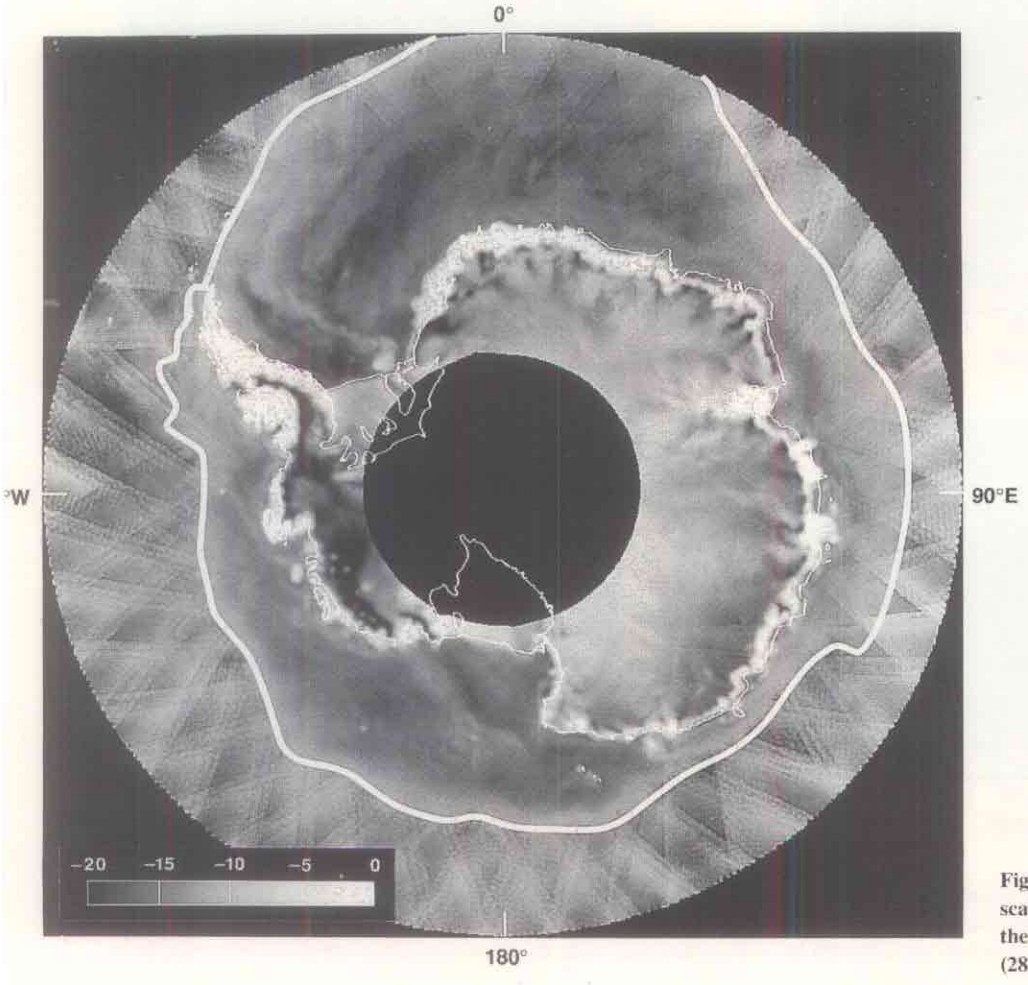

Figure 2. Reconstructed ERS-1 AMI scatterometer 14 km resolution *A* image of the Antarctic sea ice near maximum ice extent (28 Sept. − 4 Oct. 1992)

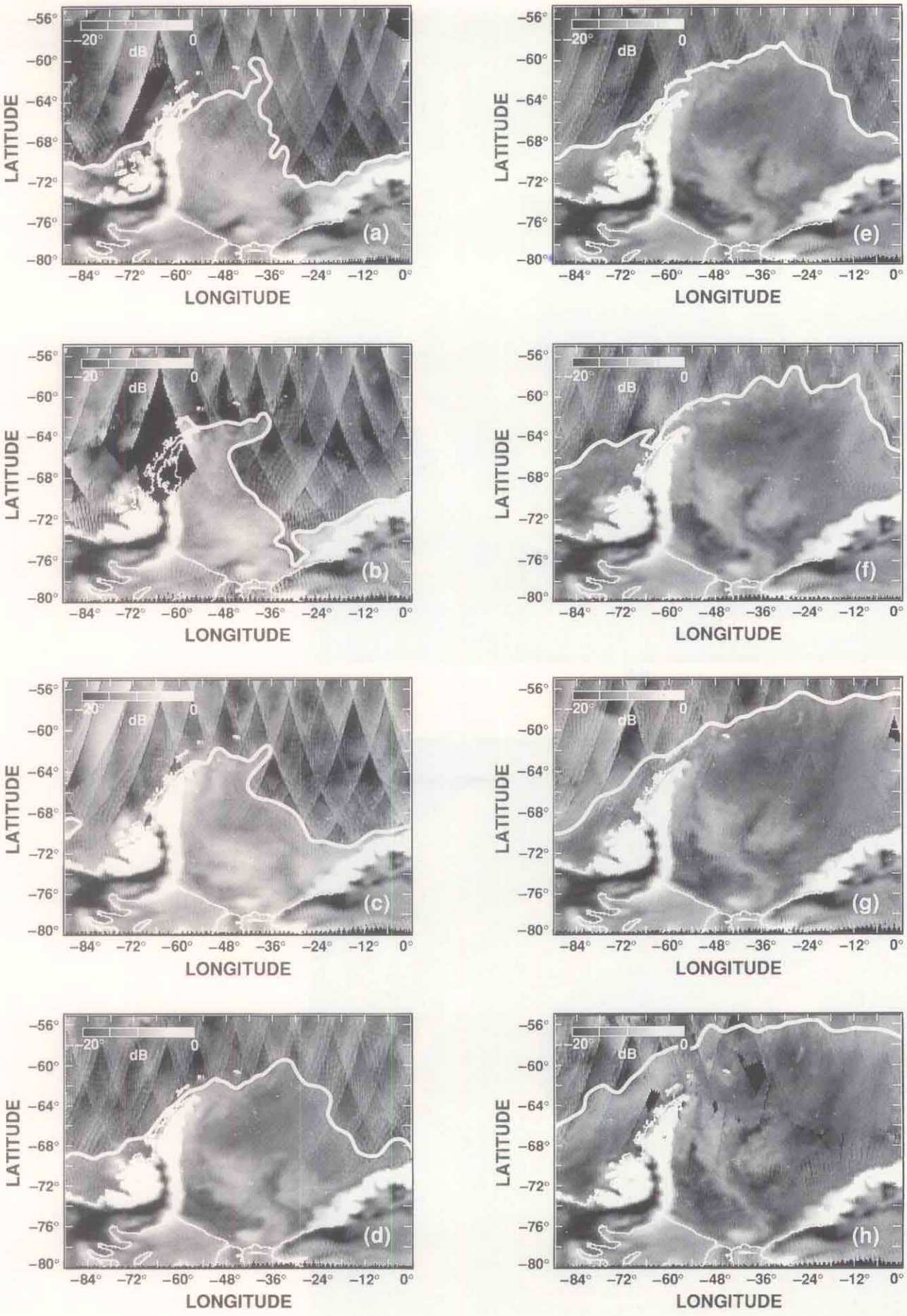

Figure 3. Weddell Sea time-series of weekly EScat *A* images, illustrating evolving backscatter characteristics of the sea-ice cover from minimum to maximum ice extent in 1992. The Julian Day periods illustrated are: (a) 32−38; (b) 53−59; (c) 74−80; (d) 104−110; (e) 125−131; (f) 146−152; (g) 167−173; (h) 188−194. Coastlines and ice shelves are indicated by a thin white line, while the sea-ice margin is identified by a thick line

Time-series maps of the Southern Ocean sea-ice cover are a primary application of the SIRF imaging technique. SAR can retrieve only limited spatial and temporal coverage of dynamic phenomena observed in response to ocean and atmosphere forcing. The scale of coverage offered by the EScat is sufficient to monitor these processes and to place the 25 m resolution 100 km $\times$100 km SAR images in the context of basin-scale ice conditions.

5. Time-series and regional sea-ice dynamics

5.1. Sea-ice advance in the Weddell Sea during the austral winter 1992

A regional time-series is shown in Figure 3 to illustrate the power of this imaging technique. Weekly *A* images are generated at 21-day intervals from the first week in February (Julian Days 32–39) in Figure 3a, through the first week in July (Julian Days 188–204) in Figure 3h. Figure 3 shows that minimum ice extent occurs at the end of February, and then indicates how the ice edge advances rapidly northeastwards by thermodynamic ice growth during the onset of austral winter. As the Weddell Sea becomes ice-bound, wind- and current-driven ice motion carries some of the large units of relatively high backscatter sea ice away from their origins along the coastal and ice shelf margins.

Of further note in Figure 3 are two polynya regions of relatively low ice concentration which appear in the early series (Fig. 3a) as two low-backscatter areas in the southern and southeastern Weddell Sea. The latter is sufficiently near to the sea-ice margin that it becomes captured in the sea-ice retreat by the end of February 1992 (Fig. 3b). Nevertheless, as the ice margin advances, these relatively low-backscatter areas reappear and become source regions for low-backscatter ice. This low-backscatter ice is transported away from these locations as it becomes entrained and advected northwestwards in the motion of the Weddell Gyre circulation.

5.2. Comparison of SASS and EScat Weddell-Sea images

A brief comparison is made here of the austral winter patterns of backscatter which developed in response to basin-wide sea-ice dynamics in 1978 and 1992. Data from 1978 Seasat SASS are used to produce *A* images illustrated in Figure 4. Comparative EScat *A* images produced for the identical periods of 1992 are shown in Figure 5.

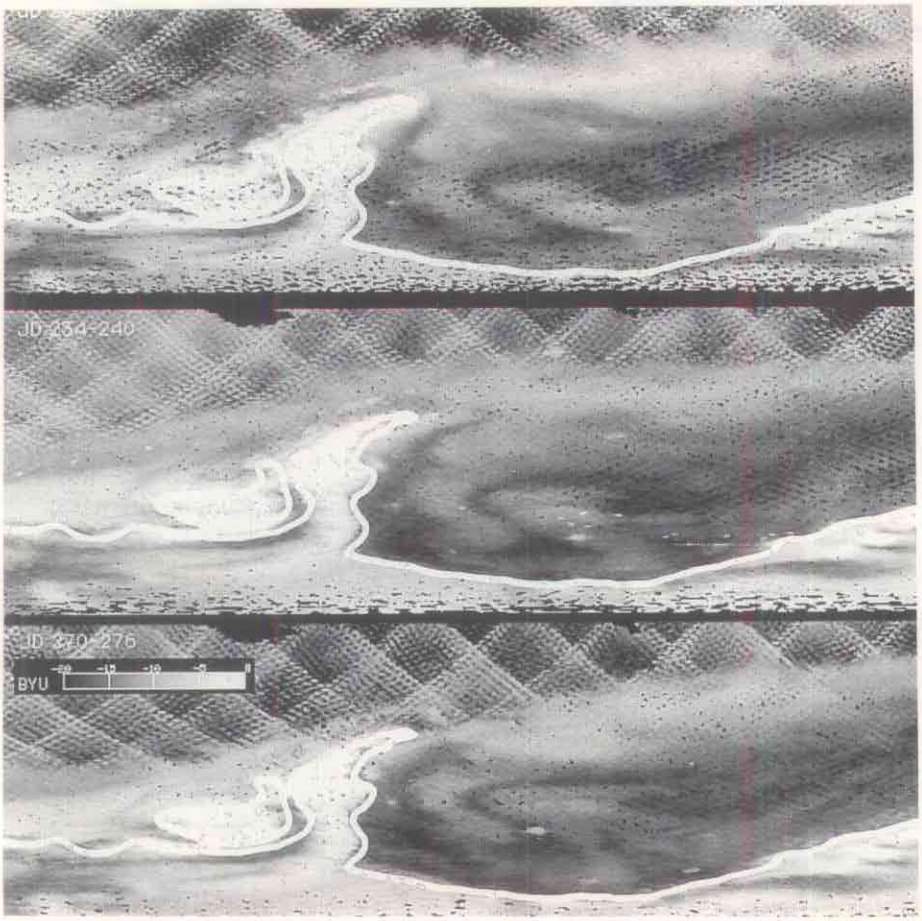

Figure 4. Seven-day *A* images of Weddell Sea ice characteristics from Seasat SASS data from the last week of the months of: (a) July (Julian Days 204–210); (b) August (JD 234–240); and (c) September (JD 270–276), in 1978. The images are shown on an equal-area Lambert projection with a longitudinal extent from −90° to 0°W and latitudinal extent from −90° to −55°S

Figure 4 images were derived from Seasat SASS data for selected 1-week periods during the 3 months of successful Seasat operation and indicate the backscatter observed by a Ku-band instrument. Figure 5 image panels extend the C-band backscatter time series shown in Figure 3.

Weekly averaged images shown in Figures 4 and 5 show month-to-month transitions in sea-ice characteristics in response to the circulation pattern of the Weddell Gyre. These indicate the situation for the last week in the months of (a) July, (b) August, and (c) September in 1978 and 1992, respectively. Gridded image data shown in Figure 4 have a higher spatial resolution than the enhanced EScat data shown in Figure 5. This enables several large icebergs to be tracked in Figure 4, such as the super-berg 'Trolltunga' seen in Figure 4c as a large bright object following the dark band in the southern central Weddell Sea. Though the ~6 km resolution achieved from Seasat SASS data is relative high, A images in Figure 4 have a large number of pixels where values of A could not be estimated (indicated as black pixels). Comparison of the SASS data in Figure 4 and EScat data in Figure 5 shows a spatial pattern of backscatter in 1978 which is almost identical to that of 1992. The images not only indicate some consistency in the imaging and resolution enhancement technique, but also in the inter-annual patterns of sea-ice circulation in the Weddell Gyre.

5.3. Ice dynamics and observed patterns of backscatter

EScat backscatter images shown in Figures 3 and 5 indicate patterns that reflect the main winter areas of ice divergence (sources for sea-ice formation) and the main areas of convergent ice (deformation and thickening regions) in the Weddell Sea. Regions with relatively low backscatter appear to be thinner undeformed ice, in contrast to the bright backscatter areas to the west of the Antarctic peninsula, along the eastern flank

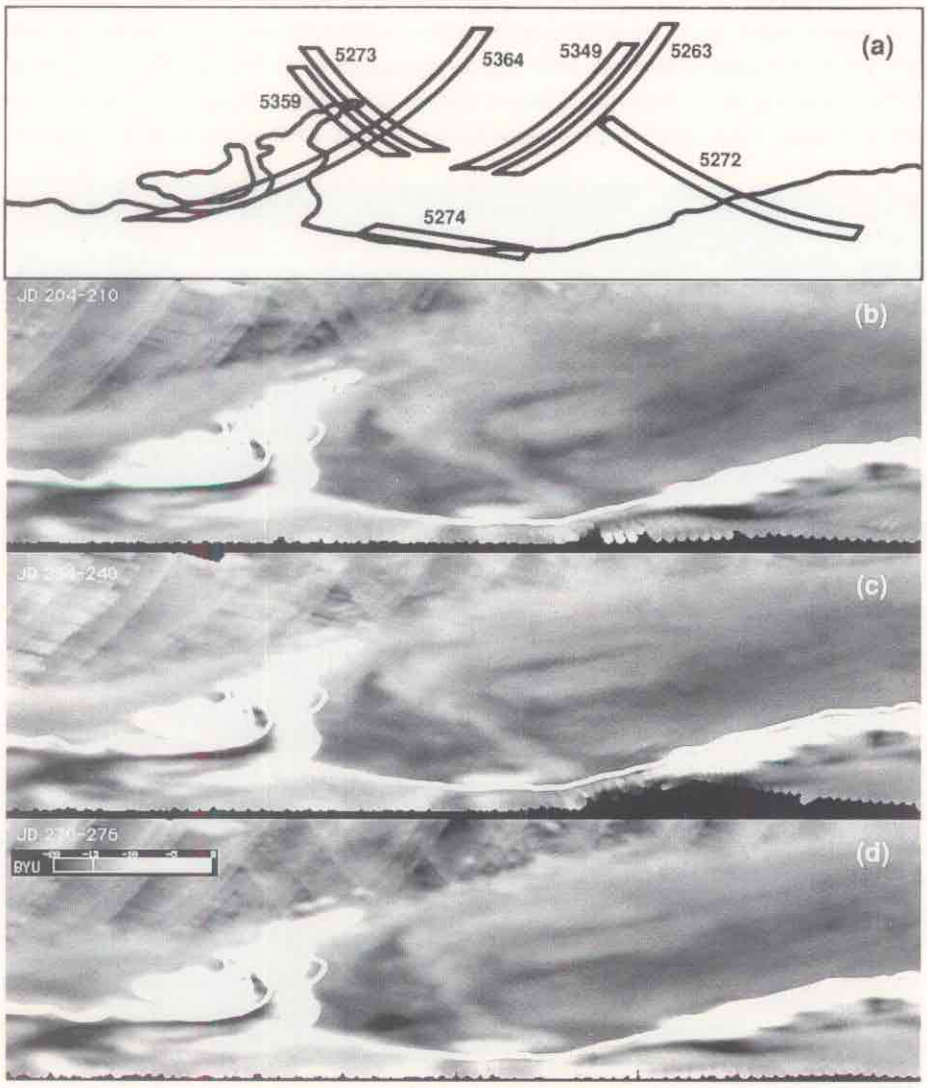

Figure 5. Comparative weekly A images of sea-ice characteristics from the ERS-1 EScat data for identical periods to those of Figure 4. Panel (a) shows a number of SAR image swaths used to illustrate ice conditions. The remaining panels show the last week in the months of: (b) July (JD 204–210); (c) August (JD 234–240); and (d) September (JD 270–276) 1992

of the northern tip of the Antarctic peninsula, and along the margin of the Filchner-Ronne ice shelf (near Berkner Island). The major source of low-backscatter ice appears to be the southern Weddell Sea, along the flank of the Filchner and Ronne ice shelves. Predominantly northward advection of sea ice, together with some vorticity introduced by the circulation within the Weddell Gyre, acts to wind these low-backscatter ice features in a clockwise direction and extend them towards the northeast.

Features observed in Figure 5 can be explained with the synergy provided by overlapping SAR images and with complimentary surface measurements. Figure 5a indicates a number of orbit swaths along which SAR data were recorded during the imaging period indicated in Figure 5b. An example from Orbit 5349 is shown in Figure 6 for a swath across some of the features in the central Gyre. This transect shows a descending orbit first crossing relatively low-concentration ice with large conglomerate floes of up to 20 km diameter in the northern marginal ice zone. Open water between these ice floes appears extremely bright due to the high wind speeds. Moving southward into more compact ice, floes become consolidated with relatively uniform low-backscatter floe units of up to 50 km diameter. In the central strip of Figure 6, the SAR crosses the narrow dark band associated with the northernmost northeast–southwest oriented dark finger in the EScat *A* image of Figure 5a. The SAR confirms this to be undeformed ice with little ridging. Of note, however, is the bright shear zone bounding the northern edge of this narrow band, and the relatively high backscatter sea-ice floe conglomerates (up to 10 km diameter) to the south, corresponding with the isolated bright patch in the centre of the Weddell Sea.

Figure 7 is a composite showing two SAR strips acquired in the northwestern Weddell Sea, near the tip of the Antarctic peninsula. These two ascending-orbit strips are indicated in Figure 5a as Orbits 5273 and 5359, and cross the margin between the relatively high-backscatter ice along the east coast of the peninsula and low-backscatter younger ice extending all the way southwards into the southwestern corner of the Weddell Sea. The two strips shown in Figure 7 clearly show the northernmost finger of relatively low-backscatter ice, which traces the path of the most rapid sea-ice drift along the edge of the continental shelf-break. High-backscatter sea ice floes are confirmed to be areas of relatively thick or deformed sea ice. It is suggested that this bright region is the last of the residual second-year ice being advected out of the Weddell Sea. Buoy drift studies undertaken during 1992, together with results from a drifting ice station (Fig. 9), confirm that the mean rate of northward drift ($\sim$10 km/d) successfully accounts for the northward translation of this southern boundary of older ice to this position in early July in Figure 5a.

Moving to the southern part of the Weddell Sea, a strip of SAR data from Orbit 5274 (Fig. 5a) shows ice conditions along the fringe of the ice shelf. Figure 4 shows a particularly bright stationary area of sea ice abutting the Filchner-Ronne ice-shelf edge, in the vicinity of Berkner Island. This ice at the western (bottom) end of the strip in Figure 8 appears to be trapped by a field of small grounded icebergs and has become well-deformed. To the north (out of this swath) is a further series of vast icebergs – A22, A23A and A23B (as documented by the US Navy/NOAA Joint Ice Center) – which further delimit the western extent of the highly deformed ice[9]. Adjacent to the compressed ice field is an extensive polynya system with relatively thinner ice. Backscatter signatures indicate a repeated series of ice-growth events mirroring the ice-shelf shape. These features show polynya formation events to have a remarkable periodicity and regularity, with the formation mechanism being strong katabatic winds which blow off the ice shelf. As each pulse of winds advects the recently formed sea ice away from the ice-shelf margin, the large polynya system remains a major source region for new sea ice in its wake. As the Gyre motion carries ice out into the Antarctic Circumpolar Current, the conveyor belt carrying these thin ice forms northwards continually renews the large low-backscatter area in the southern Weddell Sea (Figs. 3, 5b).

Figure 9 shows a typical winter synoptic 10 m surface-wind situation on 23 July (JD 205), from the European Centre for Medium-Range Weather Forecast (ECMWF) analysis fields (courtesy of Jim Maslanik, NCAR). Figure 9 also shows the drift track of the US/Russian Ice Station Weddell (ISW) as a dotted line, and the track followed

Figure 6. ERS-1 SAR Antarctic Quick-Look (SAR.AQL) 100 m resolution image strip (© ESA 1992) from Orbit 5349 in Figure 4 illustrating the variations in ice conditions along a 1941 km transect crossing the central Weddell Sea. This image was produced by the German PAF (courtesy of Jörg Gredel, DLR)

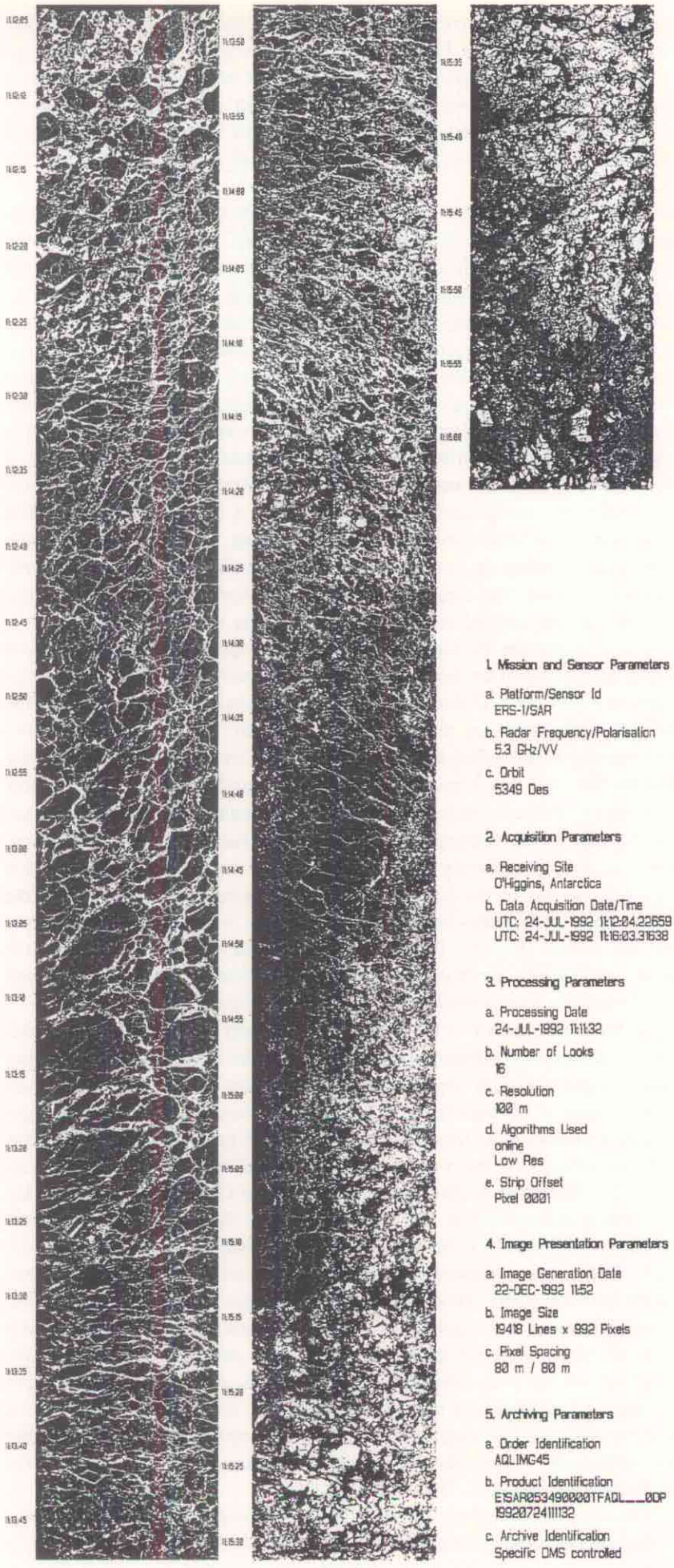

1. Mission and Sensor Parameters

a. Platform/Sensor Id
ERS-1/SAR

b. Radar Frequency/Polarisation
5.3 GHz/VV

c. Orbit
5349 Des

2. Acquisition Parameters

a. Receiving Site
O'Higgins, Antarctica

b. Data Acquisition Date/Time
UTC: 24-JUL-1992 11:12:04.22659
UTC: 24-JUL-1992 11:16:03.31638

3. Processing Parameters

a. Processing Date
24-JUL-1992 11:11:32

b. Number of Looks
16

c. Resolution
100 m

d. Algorithms Used
online
Low Res

e. Strip Offset
Pixel 0001

4. Image Presentation Parameters

a. Image Generation Date
22-DEC-1992 11:52

b. Image Size
1948 Lines x 992 Pixels

c. Pixel Spacing
80 m / 80 m

5. Archiving Parameters

a. Order Identification
AQL1MG45

b. Product Identification
E1SAR05349000TFAQL___0DP
1992072411132

c. Archive Identification
Specific DMS controlled

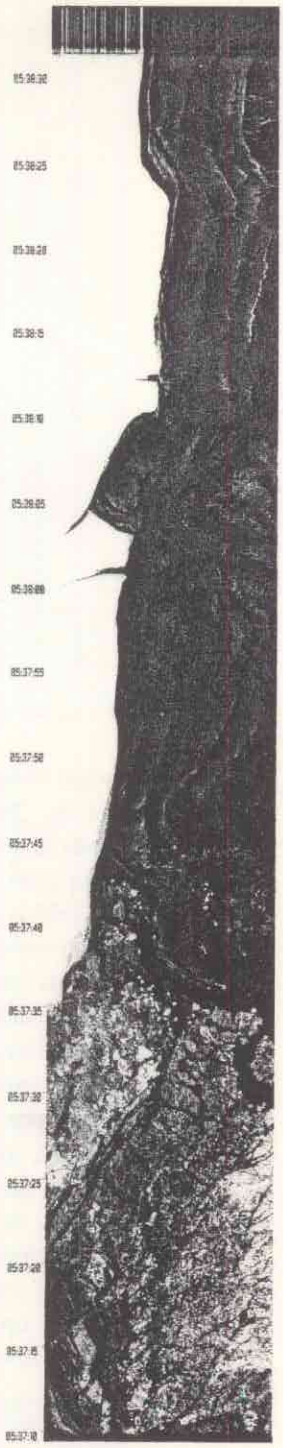

1. Mission and Sensor Parameters

a. Platform/Sensor Id
ERS-1/SAR

b. Radar Frequency/Polarisation
5.3 GHz/VV

c. Orbit
5274 Asc

2. Acquisition Parameters

a. Receiving Site
O'Higgins, Antarctica

b. Data Acquisition Date/Time
UTC: 19-JUL-1992 05:37:09.41414
UTC: 19-JUL-1992 05:38:33.71086

3. Processing Parameters

a. Processing Date
23-JUL-1992 04:41:00

b. Number of Looks
16

c. Resolution
100 m

d. Algorithms Used
replay
Low Res

e. Strip Offset
Pixel 0001

4. Image Presentation Parameters

a. Image Generation Date
22-DEC-1992 10:11

b. Image Size
6146 Lines x 992 Pixels

c. Pixel Spacing
80 m / 80 m

5. Archiving Parameters

a. Order Identification
AQLIMG41

b. Product Identification
E1SAR05274000TFAQL___0DP
19920723044100

c. Archive Identification
Specific DMS controlled

Figure 7. Pair of ERS-1 SAR Antarctic Quick-Look (SAR.AQL) images (© ESA 1992) from Orbits 5273 (acquired 19 July 1992) and 5359 (25 July 1992) across the tip of the Antarctic peninsula; produced by the German PAF (courtesy of Jörg Gredel, DLR)

Figure 8. ERS-1 SAR Antarctic Quick-Look (SAR.AQL) 100 m resolution image strip (© ESA 1992) from Orbit 5274 (acquired 19 July 1992) in Figure 4 illustrating sea-ice conditions along a 615 km transect fringing the Filchner-Ronne ice shelf. This image was produced by the German PAF (courtesy of Jörg Gredel, DLR)

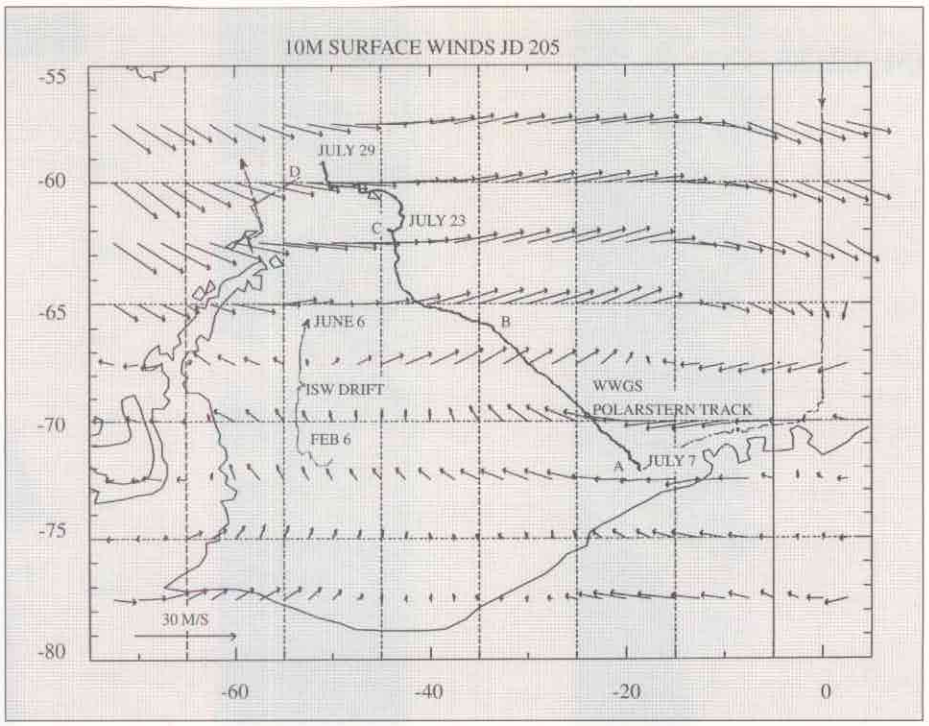

Figure 9. ECMWF analysis wind field for 12:00 Z on 23 July 1992 (JD 205), and corresponding with the synoptic situation during imaging of Figure 4b. The tracks of an Antarctic drifting ice camp and the ice breaker 'Polarstern' are indicated

by the 'Polarstern' research vessel during the Winter Weddell Gyre Study in 1992 (see Ref. 8). This typical July synoptic (austral winter) situation shows light southerly winds in the southern and central Weddell Sea, and strong July winds from the west north of 65°S. Surface wind speeds (at 10 m height) of around 15 m/s were measured at 12:00 Z onboard the R/V 'Polarstern' at the site shown on 23 July 1992 (Fig. 9) which correspond well with the analysis field speeds. These winds, and the surface currents, drive ice from the southern part of the Weddell Sea first to the north and then, at around 65°S, the stronger westerly winds coupled with the ocean currents (steered by bottom topography) turn the ice abruptly towards the northeast. The ice rapidly exits the basin to become entrained in the Antarctic Circumpolar Current, whereupon it starts to melt.

In the region between the tip of the Antarctic peninsula and the South Orkney Islands, old ice that survived the summer is evacuated from the Weddell basin. This outflow of relatively thick second-year ice was observed during ice-thickness measurements along the 'Polarstern' transect. Figure 10 shows an interpolated profile fitted to mean snow and ice depths measured on undeformed ice floes along the vessel's track, shown in Figure 9 between A (7 July 1992) and D (29 July 1992). Figure 10 clearly shows a smaller mean ice thickness and snow depth in the Eastern

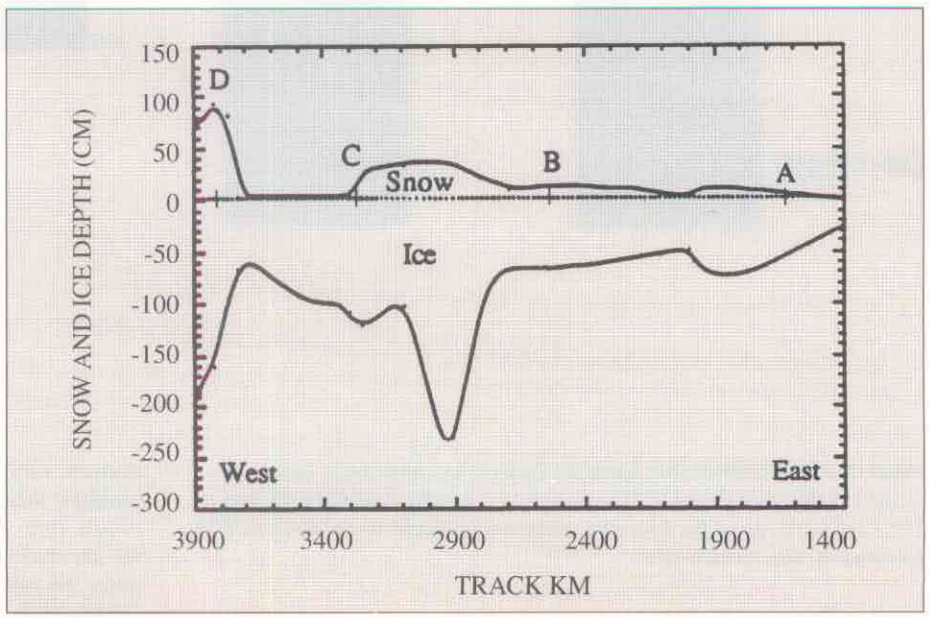

Figure 10. Snow and ice depth measurements made during the Winter Weddell Gyre Study. Each curve is interpolated to mean ice-core and snow-depth measurement points made along the track of R/V 'Polarstern'. Four key locations – A, B, C and D – are identified along the profile which correspond to the measurement sites identified in Figure 9

Weddell Sea in July (between 1400 and 2600 km). Mean snow depths of between 0 and 20 cm are typical, while the ice-thickness range of 50−80 cm is consistent with typical mean thermodynamic growth over a period of six months. Old ice first appears as the thick pulse in the profile between B and C along the transect in Figure 10. This ice, more than 2 m thick, represents the tongue of high-backscatter material, which winds it way northwards in Figure 2, Figure 3h and Figure 5 from the deformed area of ice near the Ronne-Filchner ice shelf (in Fig. 7). It ultimately exits the Weddell Sea just south of the South Orkney Islands, drifting towards the northeast. A second region of thick ice was observed at D, at the westernmost end of the transect in Figure 9. This ice is most likely a combination of outflow from the Bellingshausen Sea (to the west of the Antarctic peninsula) and ice escaping between the tip of the peninsula and the South Orkneys. An extremely deep snow cover and slightly smaller mean ice thickness characterised the old ice in these locations.

6. Conclusions

The approach discussed here for generating weekly ERS-1 sea-ice images for the entire Northern or Southern Hemisphere provides a valuable supplement to the spatially and temporally sparse higher-resolution SAR images. A relative improvement in the spatial accuracy and knowledge of the individual pulse locations within the scatterometer products would further improve the spatial and temporal resolution of these products and enable a doubling of the current resolution achieved in this paper. This would be significant in terms of feature tracking within the Antarctic ice cover, enabling tracking of sea-ice in addition to monitoring of the regional dynamics.

The main bonus of these EScat image data is: (i) the frequent coverage; and (ii) the multiple-incidence-angle observations that the technique provides. While the multiple-incidence-angle capability is not investigated here, the images of backscatter normalised to 40° incidence show a remarkable capability for monitoring basin-wide processes. Together with SAR, these medium-scale C-band backscatter images are the perfect tool for monitoring the complete Southern-Ocean sea-ice cover on a weekly basis.

While operating at a different frequency and with a slightly higher resolution than passive microwave imagers (e.g. SSM/I), these data will prove extremely powerful when used in conjunction with passive microwave images of the Antarctic ice cover. Additionally, time-series images are demonstrated to be of great value in understanding sea-ice dynamics in the Weddell Sea. When combined with surface observations from buoys and shipborne campaigns, these data help to clarify the processes of ice formation and decay in response to climatic and oceanographic forcing.

A further application of these data that can be examined in greater detail is the capability for mapping the Antarctic Ice Sheet. Seasonal and inter-annual mapping of the extent of surface melting and snow accumulation will be pursued in a similar manner to that used by Long & Drinkwater[7] on the Greenland Ice Sheet. When coupled with the radar-altimeter measurements, this information will provide valuable indications of the change in regional mass balance in response to climate.

7. Acknowledgements

We would like to thank ESA for use of the data and the JPL group for producing the gridded ERS-1 scatterometer dataset. This ESA research was carried out as one component within the PIPOR Study PIP.Ant3. Much of the work (MRD) was carried out at the Jet Propulsion Laboratory (JPL) under NASA contract, with the remainder (DGL and DSE) being conducted at Brigham Young University. We thank Robert Thomas for his support of this research project.

References

1. Lecomte P., Davidson M. & Cavanie A. 1993, Ice Boundary Mapping using ERS-1 Scatterometer Data, *ESA Earth Observation Quarterly*, No. 40, p. 8.
2. Drinkwater M.R. 1989, LIMEX '87 ice surface characteristics; implications for C-band SAR backscatter signatures. *IEEE Trans. Geosci. & Remote Sensing*, Vol. 27, No. 5, pp. 501–513.
3. Bruzzi S. 1991, The Processing and Exploitation of ERS-1 Payload Data, *ESA Bulletin*, No. 65, pp. 63–72.
4. Long D.G., Hardin P.J. & Whiting P.T. 1993, Resolution Enhancement of Spaceborne Scatterometer Data, *IEEE Trans. Geosci. & Remote Sensing*, Vol. 31, No. 3, pp. 700–715.
5. Livingstone C.E. & Drinkwater M.R. 1991, Springtime C-band SAR backscatter signatures of Labrador Sea marginal ice: measurements vs modelling predictions, *IEEE Trans. Geosci. & Remote Sensing*, Vol. 29, No. 1, pp. 29–41.
6. Long D.G. & Hardin P.J. 1993, Vegetation Studies of the Amazon Basin Using Enhanced Resolution Seasat Scatterometer Data, *IEEE Trans. Geosci. & Remote Sensing*, in press.
7. Long D.G. & Drinkwater M.R. 1993, Greenland ice sheet surface properties observed by the Seasat-A Scatterometer at enhanced resolution, *J. Glaciology*, in press.
8. Drinkwater M.R., Hosseinmostafa R. & Dierking W. 1993, Winter Microwave Radar Scatterometer Sea Ice Observations in the Weddell Sea, Antarctica, Proc. IGARSS '93 Symposium, Vol. 2, IEEE Catalog No. 93CH3294-6, pp. 446–448, 18–21 August 1993, Tokyo, Japan.
9. Zibordi G. & van Woert M.L. 1993, Antarctic Sea-Ice Mapping Using the AVHRR, *Remote Sensing of the Environment*, Vol. 45, pp. 155–163.

Manuscript received 4 November 1993